

Self-Guided Diffusion Model for Accelerating Computational Fluid Dynamics

Ruoyan Li*

liruoyan2002@g.ucla.edu
University of California, Los Angeles
Los Angeles, California, USA

Zijie Huang*

zjzhuang@cs.ucla.edu
University of California, Los Angeles
Los Angeles, California, USA

Haixin Wang

University of California, Los Angeles
Los Angeles, California, USA
whx@ucla.edu

Guancheng Wan

University of California, Los Angeles
Los Angeles, California, USA
gcwan03@ucla.edu

Yizhou Sun

University of California, Los Angeles
Los Angeles, California, USA
yzsun@cs.ucla.edu

Wei Wang

University of California, Los Angeles
Los Angeles, California, USA
weiwang@cs.ucla.edu

Abstract

Machine learning methods, such as diffusion models, are widely explored as a promising way to accelerate high-fidelity fluid dynamics computation via a super-resolution process from faster-to-compute low-fidelity input. However, existing approaches usually make impractical assumptions that the low-fidelity data is downsampled from high-fidelity data. In reality, low-fidelity data is produced by numerical solvers that use a coarser resolution. Solver-generated low-fidelity data usually sacrifices fine-grained details, such as small-scale vortices compared to high-fidelity ones. Our findings show that SOTA diffusion models struggle to reconstruct solver-generated low-fidelity inputs. To bridge this gap, we propose SG-Diff, a novel diffusion model for reconstruction, where both low-fidelity inputs and high-fidelity targets are generated from numerical solvers. We propose an *Importance Weight* strategy during training that serves as a form of self-guidance, focusing on intricate fluid details, and a *Predictor-Corrector-Advancer* SDE solver that embeds physical guidance into the diffusion sampling process. Together, these techniques steer the diffusion model toward more accurate reconstructions. Experimental results on four 2D turbulent flow datasets demonstrate the efficacy of SG-Diff against state-of-the-art baselines. Code and datasets are available at Github.

CCS Concepts

• **Applied computing** → **Physics**; • **Computing methodologies** → **Neural networks**.

Keywords

Diffusion Models, AI4Science

ACM Reference Format:

Ruoyan Li, Zijie Huang, Haixin Wang, Guancheng Wan, Yizhou Sun, and Wei Wang. 2026. Self-Guided Diffusion Model for Accelerating Computational Fluid Dynamics. In *Proceedings of the 32nd ACM SIGKDD Conference on Knowledge Discovery and Data Mining V.1 (KDD 2026)*, August 9–13, 2025.

*Equal Contribution.



This work is licensed under a Creative Commons Attribution 4.0 International License. *KDD 2026, Jeju Island, Republic of Korea.*
© 2026 Copyright held by the owner/author(s).
ACM ISBN 979-8-4007-2258-5/2026/08
<https://doi.org/10.1145/3770854.3780314>

Jeju Island, Republic of Korea. ACM, New York, NY, USA, 17 pages. <https://doi.org/10.1145/3770854.3780314>

1 Introduction

High-fidelity simulations of computational fluid dynamics (CFD) are crucial for understanding fluid interactions in engineering systems, greatly impacting design and application outcomes [38, 39]. Traditional approaches such as Direct Numerical Simulation (DNS) offer high-resolution solutions. However, they are computationally expensive, especially for turbulence with high Reynolds numbers [49]. Therefore, learning neural-based simulators from data becomes an attractive alternative, balancing between efficiency and simulation fidelity [12, 18].

One popular strategy is to reconstruct high-fidelity data from low-fidelity inputs, where the input data usually reduces the discretization grid size in the spatial domain and thus is computationally efficient [28, 36]. Various machine learning models, including those based on Convolutional Neural Networks (CNNs) [8], Generative Adversarial Networks (GANs) [16], and Diffusion Models [35, 36], have been developed to reconstruct high-fidelity CFD data from low-fidelity inputs. The majority of them are categorized as **direct mapping models**, which require both low- and high-fidelity data for training and can only capture a particular resolution mapping. In contrast, **distribution learning approaches**, such as diffusion models [36], only require high-fidelity data during training and learn the probability distribution of high-fidelity sources. Therefore, they can reconstruct from low-fidelity data at any resolution without retraining and are particularly useful when large-scale solver-generated low-fidelity data are unavailable. We compare these two approaches in Table 1.

One fundamental drawback in existing models is that low-fidelity data is artificially downsampled from high-fidelity data at the same timestamp. Such data inherently has more information compared to solver-generated low-fidelity data in reality, where coarser discretization grids are used in numerical solvers to save computational resources. As illustrated in Figure 1, the former follows “integrate then downsample”, which starts from the high-fidelity initial states to rollout trajectories, and then downsample at each timestamp. The latter follows “downsample then integrate”, which downsamples the high-fidelity initial state to obtain coarser discretization grids as starting points and rollout trajectories through numerical solvers.

Model Type	Training Data	Learning Goal	Advantages	Drawbacks	Examples
Direct Mapping	Paired low- and high-fidelity data	Learn a specific mapping from low to high fidelity data	Fast inference	Must retrain if new low-fidelity resolution differs from training	CNNs
Distribution Learning	High-fidelity data only	Capture the probability distribution of high fidelity data	Can handle low-fidelity inputs at arbitrary resolution	Slower to generate samples	Diffusion models

Table 1: Comparison of Direct Mapping and Distribution Learning Approaches

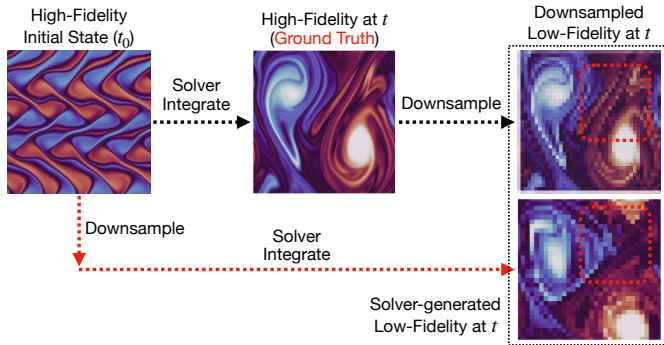


Figure 1: Comparison between downsampled (black line) and solver-generated (red line) flow fields. Solver-generated low-fidelity data retain less information, especially for fine-grained high-fidelity details.

Our experiments reveal that SOTA diffusion models struggle with solver-generated low-fidelity inputs, and we show why they fail. As a result, we study how to use **distribution learning approaches**, specifically, diffusion models, for reconstructing high-fidelity CFD data from solver-generated low-fidelity data. In response to this challenge, we build upon the state-of-the-art model proposed by Shu et al. [36] and propose an *Importance Weight* strategy during training as self-guidance to locate fine-grained high-fidelity details, and a *Predictor-Corrector-Advancer* stochastic differential equation (SDE) solver during inference for ensuring physical consistency. The two modules jointly guide the diffusion model toward higher-quality reconstructions.

Our key contributions are summarized as follows:

- **Problem Identification.** We study a novel problem on reconstructing high-fidelity flow fields with solver-generated low-fidelity data for distribution learning models. Our evidence reveals that SOTA diffusion models fail to generate high-quality outputs.
- **Practical Solution.** In light of this issue, we propose SG-Diff, a novel diffusion model with *Importance Weight* strategy during training as self-guidance and a *Predictor-Corrector-Advancer* SDE solver for physically coherent sampling.
- **Experimental Validation.** We present empirical evidence of SG-Diff’s superior performance in a variety of 2D turbulent flow over 4 datasets. It yields a significant improvement in terms of predictive accuracy, physical consistency, and perceptual quality.

2 Preliminaries and Related Work

We consider a machine learning model $f_\theta : \mathcal{X} \rightarrow \mathcal{Y}$ with parameters θ , which transforms a data sample from low-fidelity domain $x \in \mathcal{X} \subseteq \mathbb{R}^{m \times m}$ to high-fidelity domain $y \in \mathcal{Y} \subseteq \mathbb{R}^{n \times n}$ ($m < n$). The distributions of the training and test sets for low-fidelity data are denoted by $p_{\mathcal{X}}^{\text{train}}$ and $p_{\mathcal{X}}^{\text{test}}$, respectively, and for high-fidelity data as $p_{\mathcal{Y}}^{\text{train}}$ and $p_{\mathcal{Y}}^{\text{test}}$. The objective is to develop f_θ such that it can effectively map samples from $\mathcal{X}^{\text{test}}$ to their corresponding high-fidelity counterparts $\mathcal{Y}^{\text{test}}$. As diffusion model operates on the same input and output grid, we upsample the low-fidelity data uniformly during inference as the model input.

2.1 AI for Computational Fluid Dynamics (CFD)

Flow Field Reconstruction In the field of high-fidelity CFD reconstruction, researchers have developed powerful models rooted in image super-resolution domain in computer vision. For example, Jiang et al. [13], Ren et al. [30] leveraged CNN for spatial-temporal super-resolution. Li and McComb [16] further advanced the field by proposing physics-informed GANs. Additionally, Fu et al. [7] proposed a refinement network to address the issue with limited high-fidelity data. These models rely on low- and high-fidelity data pairs during training and can only capture specific resolution mappings. As a result, Shu et al. [36] leveraged diffusion model, which is trained exclusively on high-fidelity data and enables reconstruction from any low-fidelity input at any resolution. However, their experiments assume the low-fidelity data is artificially downsampled from high-fidelity sources, which leads to unreliable results. Sarkar et al. [34] evaluate direct mapping models that are trained and tested on solver-generated low-fidelity data. These approaches depend on large collections of low- and high-fidelity pairs from numerical solvers for training, and degrade once the low-fidelity inputs deviate from their training distribution.

PDE Simulation Recent advances in AI for PDE simulation include neural operator approaches like DeepONet [22] and Fourier Neural Operators [19], which learn mappings between infinite-dimensional function spaces to generalize across discretizations. Extensions such as Physics-Informed Neural Operators [20] incorporate PDE structure into training. Latent generative models have also emerged: Text2PDE [50] applies diffusion models conditioned on text prompts, while flow-matching accelerates high-resolution forecasting [43]. MultiPDENet [40] integrates Runge-Kutta schemes with learnable convolutions for long-term accuracy on fluid dynamics tasks.

¹For direct mapping models, the training takes low- and high-fidelity pairs as inputs. For diffusion models such as Shu et al. [36], the training only requires high-fidelity data, and low-fidelity data is used as input during testing.

2.2 Diffusion Model

Diffusion models have become a prominent class of deep generative models, demonstrating state-of-the-art performance across various domains such as image generation [10, 17, 26, 32], video synthesis [45, 46], and applications in scientific fields [29, 36, 44]. Diffusion models are grounded in a stochastic diffusion process, akin to those found in thermodynamics. It contains a forward and reverse process, where a data sample is gradually corrupted with noise, and a neural network is trained to reverse this. The forward process is defined by the SDE:

$$dx = f(x, t)dt + g(t)dW_t, \quad x_0 \sim p_{\text{data}}(x), \quad (1)$$

where $f(x, t)$ is the drift function, $g(t)$ is a time-dependent diffusion coefficient, and dW_t is Brownian motion. $t \in [0, T]$ is a continuous time variable with $t = 0$ corresponding to original data and $t = T$ corresponding to pure noise. The reverse diffusion is given by

$$dx = [f(x, t) - g(t)^2 \nabla_x \log p_t(x)] dt + g(t) d\bar{W}_t, \quad (2)$$

where $\nabla_x \log p_t(x)$ is the score function of the intractable marginal distribution and $d\bar{W}_t$ is the reverse-time Brownian motion. We leverage a parametrized score model $s_\theta(x_t, t)$ to estimate the score function and use the score matching objective [37] for training:

$$\mathbb{E}_{t, x_0, x_t} [\lambda(t) \|s_\theta(x_t, t) - \nabla_{x_t} \log p_t(x_t | x_0)\|^2], \quad (3)$$

where $t \sim \text{Uniform}(0, T)$ and $x_t \sim p(x_t | x_0)$.

Diffusion Model for Linear Inverse Problem Diffusion models have become a powerful class of priors for solving linear inverse problems such as image super-resolution. Early works like DiffPIR [51] and ILVR [3] introduced plug-and-play frameworks where a pre-trained unconditional diffusion model is conditioned post hoc. Building on this, DPS [4] leverages a posterior sampling formulation to guide the reverse process using a likelihood score. More efficient variants have emerged, including ResShift [47], which modifies the diffusion trajectory to accelerate sampling, and RePaint [23], which introduces re-noising steps for temporal consistency. In super-resolution specifically, methods like SR3 [33] and DDNM [41] push toward task-specific designs or refinement strategies to enhance quality or controllability.

3 Method:SG-Diff

We build upon the diffusion framework proposed by Shu et al. [36] and study reconstructing high-fidelity data from solver-generated low-fidelity inputs, which have more information loss compared to artificially downsampled low-fidelity inputs. Our model, SG-Diff, features an *Importance Weight* strategy that scores different components in the flow fields through the loss function in a self-supervised manner, forcing the model to recover more fine-grained high-fidelity details during training. In addition, a *Predictor-Corrector-Advancer* SDE solver applies physics-informed correction during sampling, ensuring physical coherence in reconstructed samples during inference. The two modules jointly guide the model toward high-quality reconstruction from a wide range of low-fidelity inputs. The overall framework is depicted in Figure 2. We now introduce each component in detail.

Model Setup. SG-Diff follows the guided data synthesis setting as in Meng et al. [26], Shu et al. [36]: we train the model with high-fidelity sources only, and condition on low-fidelity inputs as

intermediate diffusion step during inference. This brings two benefits: (1) exerting control over the reconstruction process during inference. Instead of starting from random noises, the reverse diffusion starts from low-fidelity inputs as intermediate diffusion steps. (2) The model can reconstruct from generalized low-fidelity data, since the training does not depend on low- and high-fidelity pairs as in direct mapping models such as CNNs.

Formally, during the forward training process, we obtain intermediate diffusion states x_t by solving the following forward SDE. We adopt VP-SDE [10], where $f(x, t) = -\frac{1}{2}\beta_t x_t$, $g(t) = \sqrt{\beta_t}$, and $\{\beta_1, \dots, \beta_T\}$ are variance schedules. The forward procedure continuously adds noises to the high-fidelity sample x_0 .

$$dx_t = f(x_t, t)dt + g(t)dW_t, \quad x_0 = y \sim p_y^{\text{train}}. \quad (4)$$

During inference stage, instead of starting from $x_T \sim N(0, I)$, we obtain the intermediate diffusion state $x_{t_{\text{guide}}}$ ($0 < t_{\text{guide}} < T$) by adding noises to the conditioned low-fidelity data $x \sim p_x^{\text{test}}$ as

$$x_{t_{\text{guide}}} = x + \int_0^{t_{\text{guide}}} f(x_s, s) ds + \int_0^{t_{\text{guide}}} g(s) dW_s. \quad (5)$$

We adopt the same t_{guide} as Shu et al. [36], and use $x_{t_{\text{guide}}}$ as the starting point for the reverse process to reconstruct the high-fidelity sources. Then, we solve the reverse SDE in Equation 2 to progressively produce a refined high-fidelity reconstruction that aligns with the low-fidelity conditioning data. Shu et al. [36] applied the above procedure to reconstruct high-fidelity data from artificially downsampled low-fidelity input. We demonstrate in Proposition 3.1 why their proposed diffusion model performs poorly for solver-generated low-fidelity data. For solver-generated low-fidelity data, the differences in noised probability distributions become larger, which hinders diffusion model’s ability for accurate reconstruction.

Proposition 3.1. *Let p_y denote the probability distribution of high-fidelity data. Let p_x and q_x denote the probability distribution of solver generated and downsampled low-fidelity data respectively. Define \tilde{p}_y , \tilde{p}_x , and \tilde{q}_x to be the probability distribution transformed from p_y , p_x , and q_x by applying Equation 5. Then, it follows that $D_{KL}(\tilde{p}_y \| \tilde{p}_x) \geq D_{KL}(\tilde{p}_y \| \tilde{q}_x)$.*

3.1 Importance Weight During Training

We therefore introduce an importance weighting mechanism during training as self-guidance to ensure accurate reconstruction of fine-grained details. Specifically, we transform the high-fidelity data into the wavelet domain using the DWT and assign importance scores to different components of fluid fields within the diffusion loss function. By considering spatial relationships between nearby vorticity, DWT has great abilities to locate information both in spatial and frequency domains [1, 6], thus allowing the model to capture fine-grained structures effectively. Formally, we decompose fluid fields $y \in \mathcal{R}^{n \times n}$ into frequency subdomains and compute the sum of squares of the high-frequency modes – namely HL (high-low), LH (low-high) and HH (high-high) subdomains as below, where $HL, LH, HH, F \in \mathbb{R}^{\frac{n}{2} \times \frac{n}{2}}$. HL captures horizontal high-frequency signals, while LH captures vertical high-frequency signals. HH captures high-frequency signals in both directions, corresponding to diagonal details such as intersections.

$$F = HL^2 + LH^2 + HH^2. \quad (6)$$

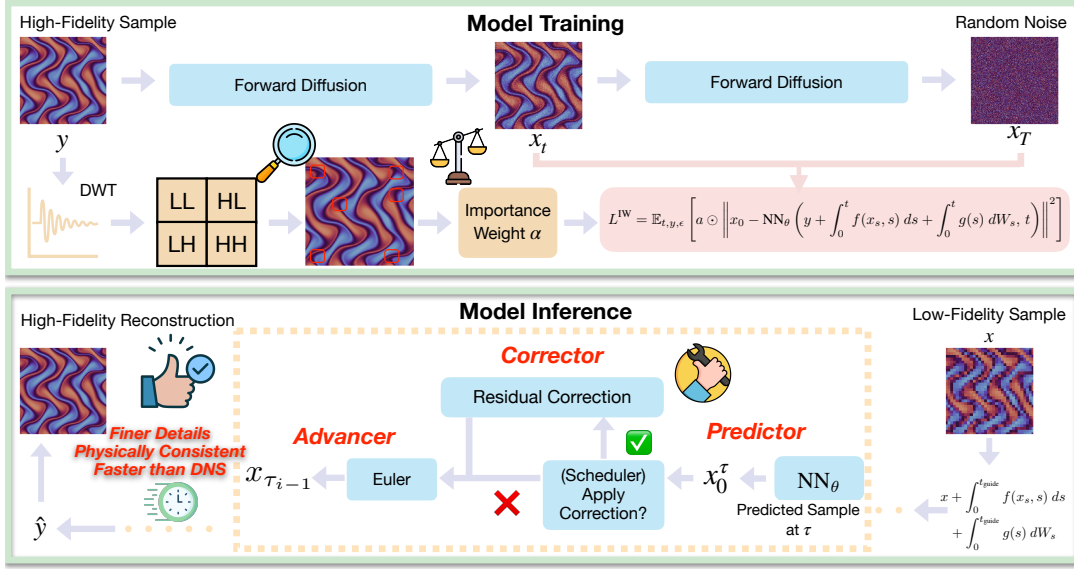


Figure 2: Training and inference pipeline of SG-Diff. Training with high-fidelity data only, guided by Importance Weight strategy to locate fine-grained high-fidelity details. During inference, low-fidelity data is used as guidance, and the Predictor-Corrector-Advancer solver ensures physical coherence.

To compute importance scores, we then uniformly upsample F to $\hat{F} \in \mathbb{R}^{n \times n}$ and linearly map $\hat{F}_{i,j}$ to an importance weight $a_{i,j}$ as below, where α, β are the minimum and maximum importance weight value respectively, $Q_\theta(\hat{F}) \in \mathbb{R}$ is the θ quantile of all \hat{F} values.

$$a_{i,j} = \begin{cases} \alpha + (\beta - \alpha) \frac{\hat{F}_{i,j} - Q_\theta(\hat{F})}{\max \hat{F} - Q_\theta(\hat{F})} & \text{if } \hat{F}_{i,j} > Q_\theta(\hat{F}) \\ 1 & \text{otherwise} \end{cases} \quad (7)$$

If $\hat{F}_{i,j}$ exceeds the θ quantile of all \hat{F} values, the corresponding component is considered high-frequency, and will be assigned with weight greater than 1. Finally, the diffusion loss function in Eqn 3 is updated to incorporate the importance weighting. Note that our diffusion models directly predict the denoised sample instead of noise or score.

$$L^{IW} = \mathbb{E}_{t,y,\epsilon} \left[a \odot \left\| x_0 - \text{NN}_\theta \left(y + \int_0^t f(x_s, s) ds + \int_0^t g(s) dW_s, t \right) \right\|^2 \right], \quad (8)$$

where x_0 represents the ground truth high-fidelity sample, NN_θ predicts the denoised high-fidelity sample, and \odot denotes element-wise multiplication.

Importance Weight Design Choice. Our importance weight strategy is incorporated exclusively during training. The DWT-based calculation avoids the large computational complexity often associated with attention mechanisms. It efficiently emphasizes important features by leveraging the intrinsic properties of the wavelet transform, resulting in a more targeted learning process.

Generalization of Hyperparameters The quantile θ , and the minimum and maximum importance weight values α, β are tuned using only one dataset and generalize to all others.

3.2 Predictor-Corrector-Advancer SDE Solver

In addition, we introduce a *Predictor-Corrector-Advancer* SDE solver to enhance the physical coherence of the reconstructed data during inference. In the reverse diffusion process, the *Predictor* first generate predicted high-fidelity data $\hat{x}_0^t = \text{NN}_\theta(x_t, t)$. Then, the *Corrector* applies residual corrections to \hat{x}_0^t to enhance physical consistency. Let \mathcal{L} be a differential operator associated with a PDE acting on a function $u : \Omega \rightarrow \mathbb{R}^{n \times n}$, defined on a domain $\Omega \subset \mathbb{R}^{n \times n}$, with source term $f : \Omega \rightarrow \mathbb{R}^{n \times n}$. The PDE is expressed as $\mathcal{L}u(x) = f(x)$, $x \in \Omega$. Given an approximate solution $\tilde{u}(x)$, the PDE residual $\mathcal{R}(x)$ is defined as $\mathcal{R}(x) := \|\mathcal{L}\tilde{u}(x) - f(x)\|_2^2$. The correction is to perform M steps gradient descent based on the residuals using the Adam algorithm [15]. Finally, the *Advancer* leverages Euler-Maruyama [24] to advance to the next diffusion step. The inference procedure is summarized in Algorithm 1.

We begin by analyzing the convergence properties of the *Corrector*. Proposition 3.2 suggests that increasing the number of gradient descent steps generally leads to smaller residual values. Thus, for optimal physical consistency, Proposition 3.2 suggests to perform more gradient descent steps, i.e. larger M .

Proposition 3.2 (Regret Bound of *Corrector* (Kingma and Ba [15] Corollary 4.2)). Define the regret $r(M) = \sum_{i=1}^M [\mathcal{R}(x_i) - \mathcal{R}(x^*)]$, where $x^* = \arg\min_x \sum_{i=1}^M \mathcal{R}(x)$. Assume $\mathcal{R}(x)$ has bounded gradient and distance between any x_i generated by Adam is bounded. The *Corrector* achieves the following guarantee, for all $M \geq 1$: $\frac{r(M)}{M} = O\left(\frac{1}{\sqrt{M}}\right)$.

We then introduce the error bound for our *Predictor-Corrector-Advancer* SDE solver in Proposition 3.3, with proof detailed in Appendix H. The derived bound indicates that, under finite temporal

Algorithm 1 Predictor-Corrector-Advancer Inference Algorithm.

Require: $x \in \mathcal{X}^{\text{test}}$, t_{guide} , $\tau = \{\tau_0, \tau_1, \dots, \tau_K\}$ (backward steps, where $\tau_0 = 0, \dots, \tau_K = t_{\text{guide}}$), NN_θ , $\mathcal{R}(\cdot)$, M (gradient descent steps), η (step size).

```

1:  $x_{\tau_k} = x + \int_0^{\tau_k} f(x_s, s) ds + \int_0^{\tau_k} g(s) dW_s.$ 
2: for  $i = K, K-1, \dots, 1, 0$  do
3:   Predictor:  $\tilde{x}_0^{\tau_i} = \text{NN}_\theta(x_{\tau_i}, \tau_i)$ 
4:   if correction is performed at time  $\tau_{i-1}$  then
5:     repeat
6:       Corrector:  $\hat{x}_0^{\tau_i} = \tilde{x}_0^{\tau_i} - \eta \cdot \text{Adam}(\nabla \mathcal{R}(\tilde{x}_0^{\tau_i}))$ 
7:     until  $M$  times
8:   end if
9:   Advancer:  $x_{\tau_{i-1}} = x_{\tau_i} + \left[ f(x_{\tau_i}, \tau_i) + g^2(\tau_i) \frac{x_{\tau_i} - \tilde{x}_0^{\tau_i} - \int_0^{\tau_i} f(x_s, s) ds}{\int_0^{\tau_i} g^2(s) dW_s} \right] dt + g(t) d\bar{W}_{\tau_i}$ 
10: end for

```

discretization Δt , (1) an increase in the correction region, $|A|$, could lead to an increase in the prediction error; and (2) a higher number of gradient descent steps, M , similarly could result in larger predictive error. This observation is noteworthy because, while Proposition 3.2 demonstrates that a larger M enhances the physical consistency, Proposition 3.3 simultaneously reveals that it adversely affects predictive accuracy. Consequently, these findings highlight the importance of balancing the competing influences of physical consistency and prediction accuracy. To address such trade-off, Section 4.4 investigates into (1) determining an optimal schedule for applying the correction; and (2) establishing the optimal frequency of correction.

Proposition 3.3 (Error Bound for *Predictor-Corrector-Advancer*). *Let \hat{x}_t denotes the piecewise solution of x_t solved using the Predictor-Corrector-Advancer method. Then,*

$$Z(T) = \sup_{0 \leq s \leq T} \mathbb{E} [|x_s - \hat{x}_s|^2] \leq O(\Delta t \exp(O(|A|^2(1 + \eta L_Q L_{\mathcal{R}})^{2M}))), \quad (9)$$

where $\eta, L_Q, L_{\mathcal{R}}$ are positive constant. A denotes the region where correction is applied and B otherwise. $A \cup B = [0, T]$ and $A \cap B = \emptyset$.

Additionally, we notice that the expected error approaches zero as the time discretization Δt approaches zero. This implies the strong and weak convergence of our method.

Proposition 3.4 (Strong and Weak Convergence of *Predictor-Corrector-Advancer* SDE Solver). *The SDE solver outlined in Algorithm 1 satisfies both strong and weak convergence. Namely, for any appropriate test function ϕ .*

$$\lim_{\Delta t \rightarrow 0} \sup_{0 \leq s \leq T} \mathbb{E} [|x_s - \hat{x}_s|^2] = 0 \quad (\text{Strong Convergence}) \quad (10)$$

$$\lim_{\Delta t \rightarrow 0} | \mathbb{E} [\phi(\hat{x}_{t_N})] - \mathbb{E} [\phi(x_T)] | = 0 \quad (\text{Weak Convergence}) \quad (11)$$

The strong convergence implies the sample paths of the numerical approximation approach those of the true process in a mean sense. Equivalently, the error measured pathwise becomes arbitrarily small. Weak convergence is a result of strong convergence, and it guarantees the target distributions of the approximations converge.

Generalization of Correction Schedule The correction schedule and number of gradient descent steps are tuned using only one dataset and generalize to all others.

Availability of PDE Residual Our approach is designed to work in tandem with numerical PDE solvers, which require a complete specification of the PDE: its functional form, parameters, and boundary conditions. Consequently, it is reasonable to assume that the PDE residual is available.

Contribution of Predictor-Corrector-Advance Solver While the use of PDE residuals in neural networks is well established, we introduce a novel mechanism for injecting them into diffusion models. Huang et al. [11] and Bastek et al. [2] also embed PDE residuals in diffusion models. The former injects the residual's gradient into the score, while the latter adds the residual to the loss function. **We instead apply several Adam updates to the predicted clean sample at selected reverse-diffusion steps. This design is motivated by the trade-off between residual minimization and denoising performance as demonstrated by the error bound. Furthermore, in the experiment sections, we identify the scheduling policy that optimally balances these two objectives and demonstrate that it outperforms all baselines.** For comparison, we combine the residual score guidance of Huang et al. [11] with the vanilla model of Shu et al. [36] to create a Residual Score-Guided Diffusion (RSGD) baseline and also include the residual-loss approach of Shan et al. [35] during experiments.

3.3 Connection to Diffusion Posterior Sampling

Diffusion models have shown great performance in image super-resolution tasks [4, 14, 31, 51]. These studies assume that for high-fidelity data y and low-fidelity data x , there exists \mathcal{A} such that $x = \mathcal{A}(y) + \epsilon$, where ϵ is random noise. While this holds for straightforward downsampling, our solver-generated low-fidelity data can only approximate by

$$\mathcal{A}(y) \approx \text{ForwardSolver}(\text{Downsample}(\text{ReverseSolver}(y, t_{\text{fluid}}), t_{\text{fluid}}),$$

$\text{ReverseSolver}(y, t_{\text{fluid}}))$ integrates backward to estimate the initial high-fidelity state, which is downsampled and used by ForwardSolver to produce the low-fidelity data. Computing gradients with respect to A is impractical due to adaptive time stepping resulting in tens of thousands iterations for numerical solvers. As a result, previous approaches cannot be directly applied, but we still include some

		DiffPIR	DPS	ResShift	PiRD	RSGD	Diff	Cond Diff	SG-Diff	SG-Diff w/o Cor	SG-Diff w/o IW
<i>Taylor Green Vortex</i>	L2	7.09	7.08	3.57	3.97	4.50	3.28	4.50	3.18	3.20	3.22
	Res.	1434447.8194	1434333.5481	0.0426	0.9973	0.3892	51.5538	0.5392	0.0016	184.5116	0.1306
	L2	6.84	6.83	1.73	2.20	2.53	1.68	3.57	1.55	1.57	1.59
	Res.	1451893.9373	1451604.5279	0.1431	0.9912	7356.7753	25.0334	778.6521	0.0196	145.8101	0.0377
<i>Decaying Turbulence</i>	L2	3.89	3.89	1.99	2.00	1.91	1.84	2.02	1.71	1.71	1.72
	Res.	243726.9497	243724.2074	0.3971	0.9222	3178.7928	2111.2344	26592.0857	0.0488	13.2799	0.1164
	L2	3.51	3.51	0.93	0.96	0.87	0.85	1.34	0.79	0.81	0.81
	Res.	229694.9224	251006.8961	0.3935	0.9220	1363.2269	375.9871	4994.4697	0.0059	21.3210	0.0143
<i>Kolmogorov Flow</i>	L2	7.09	7.08	2.90	2.95	3.06	3.09	3.13	2.78	2.82	2.93
	Res.	452127.1843	449397.5745	104.3518	0.8137	0.08677	9.5772	0.6837	0.0082	199.9087	0.0803
	L2	7.08	7.07	1.97	1.94	1.75	1.79	1.79	1.61	1.69	1.73
	Res.	452127.4891	449315.7908	95.9227	0.8754	1.3277	36.2915	7.6139	0.0135	41.1452	0.3039
<i>McWilliams Flow</i>	L2	4.37	4.36	2.27	2.28	2.33	2.23	2.24	2.04	2.06	2.16
	Res.	54584.1591	54307.2485	0.1521	0.6638	0.5602	2.0254	0.8247	0.0291	79.9192	0.0305
	L2	4.36	4.36	1.44	1.43	1.45	1.29	1.30	1.24	1.27	1.30
	Res.	58511.5298	54284.0874	0.1068	0.6613	0.6371	5.0219	13.7145	0.0017	150.1363	0.6516

Table 2: Quantitative performance comparison over four datasets on L2 and Res metrics. Rows with a gray background report results for $32 \times 32 \rightarrow 256 \times 256$ tasks, while rows with a white background report results for $64 \times 64 \rightarrow 256 \times 256$ tasks. Columns highlighted in yellow show results for our model and its ablations. Bold values indicate the best performance in each row.

as baselines due to their prominence in related tasks. In our experiments, we adopt a downsampling strategy for \mathcal{A} following [4].

To incorporate low-fidelity data into the reverse diffusion process, we follow Shu et al. [36] by treating the low-fidelity data as intermediate reverse diffusion samples. We contend that this strategy offers stronger guidance. Although the gradient guidance from previous works facilitates projection onto the measurement subspace, our problem is characterized by a focus on a hard L2 loss, thereby requiring convergency to exact target point. As demonstrated in the experimental section, Chung et al. [4], Zhu et al. [51] often produce significantly larger L2 loss.

4 Experiments

4.1 Dataset

We generate four 2D turbulent flow datasets using the incompressible Navier-Stokes: 1.) *Taylor Green Vortex*, featuring gradually break down of large-scale vortices into smaller turbulent structures; 2.) *Decaying Turbulence*, describing turbulence that evolves naturally without external forces; 3.) *Kolmogorov Flow*, portraying turbulence influenced by a sinusoidal external force; 4.) *McWilliams Flow* [25], describing the behavior of isolated vortices in turbulent conditions.

$$\frac{\partial \omega(\mathbf{x}, t)}{\partial t} + \mathbf{u}(\mathbf{x}, t) \cdot \nabla \omega(\mathbf{x}, t) = \frac{1}{Re} \nabla^2 \omega(\mathbf{x}, t) + f(\mathbf{x}),$$

$$\nabla \cdot \mathbf{u}(\mathbf{x}, t) = 0, \quad \omega(\mathbf{x}, 0) = \omega_0(\mathbf{x}),$$

where ω represents vorticity, \mathbf{u} denotes velocity field, Re is the Reynolds number, and $f(\mathbf{x})$ is an external forcing. ω_0 represents the initial vorticity distribution. The PDE is numerically solved by pseudo-spectral solver [27] on equispaced discretization grids. The

high-fidelity data are generated with 4096×4096 grid and then uniformly downsampled to 256×256 , while those on the lower-resolution grids are considered low-fidelity. The *Taylor–Green Vortex* dataset contains 100 trajectories of 192 time steps at a Reynolds number of 1000. The *Decaying Turbulence* dataset contains 400 trajectories of 64 time steps at a Reynolds number of 450. The *Kolmogorov Flow* dataset contains 50 trajectories of 320 time steps at a Reynolds number of 1000. The *McWilliams Flow* dataset contains 50 trajectories of 320 time steps at a Reynolds number of 2000. Each dataset is split with 80 percent of the trajectories for training, 10 percent for validation, and 10 percent for testing. We refer the readers to Appendix A for additional details.

4.2 Experiment Settings

Task Setup and Baselines. We evaluate two reconstruction settings: $64 \times 64 \rightarrow 256 \times 256$ ($4 \times$ upsampling) and $32 \times 32 \rightarrow 256 \times 256$ ($8 \times$ upsampling). We compare against seven diffusion based reconstruction models: ResShift [47], PiRD [35], DiffPIR [51], Diffusion Posterior Sampling (DPS) [4], Residual Score Guided Diffusion (RSGD) [11], Vanilla Diffusion (Diff) and its conditional variant (Cond Diff) from Shu et al. [36]. We perform two ablation studies, namely SG-Diffw/o IW and SG-Diffw/o Cor, where we remove *Importance Weight* and *Predictor-Corrector-Advancer* respectively. The comparisons between direct mapping models are available in Shu et al. [36] and Appendix B.

Evaluation Metrics. We assess the reconstructed flow fields using L2 norm for measuring the pointwise error and normalized residual errors (Res.) for assessing adherence to the underlying physics. According to Shu et al. [36], lower residual values indicate

enhanced physical consistency. Given that the high-fidelity residuals are also nonzero, we posit that reconstructed samples whose residuals more closely match those of the high-fidelity data are superior. The nonzero residuals observed in high-fidelity data can be attributed to the inherent approximations in residual computation with downsampled high-fidelity data, as well as the irreducible error present in numerical approximation. Formally, the metric is defined as $\frac{(\mathcal{R}(\hat{x}_0) - \mathcal{R}(y))^2}{\mathcal{R}(y)^2}$, where \hat{x}_0 is the predicted reconstruction and y is the ground truth.

In addition, we conduct a novel multi-scale evaluation using DWT: we transform the predicted and ground truth flow fields into wavelet space and decompose them into four subdomains: LL, LH, HL, and HH. The LL subdomain captures large-scale, low-frequency information, while LH, HL, and HH encompass higher-frequency details like turbulent structures. By calculating the L2 norm in each subdomain, we gain a comprehensive understanding of the model’s performance across different scales, ensuring accurate reconstruction of both global flow features and fine-scale details.

Method	HH	HL	LL	LH
DiffPIR	4.3914	9.0811	188.6012	3.6674
DPS	4.3978	9.0713	187.9728	3.6626
ResShift	0.1164	1.6399	13.4812	1.9845
PiRD	0.1093	1.6150	12.9042	1.9455
RSGD	0.0336	0.2134	13.5701	0.4348
Diffusion	0.0279	0.2437	14.0867	0.4011
Cond Diff	0.0294	0.2476	14.1269	0.4137
SG-Diff	0.0263	0.2103	12.0338	0.3216

Table 3: Kolmogorov Flow 4× Upsampling

4.3 Reconstruction Results

Table 2 reports the L2 loss and PDE residual across datasets and models. For both upsampling scales, SG-Diff consistently outperforms baselines, showing its effectiveness. The lower L2 achieved by SG-Diff indicates that it effectively captures essential features and dynamics of the turbulent flows. Additionally, residuals from SG-Diff reconstructions are closer to those of the high-fidelity data. The small difference in PDE residuals indicates that SG-Diff’s predictions adhere more closely to the underlying physical laws. For complex datasets dominated by fine-grained details, such as *Kolmogorov Flow* and *McWilliams Flow*, SG-Diff outperforms baselines by a margin, showing better reconstruction accuracy and physical coherence. Through ablation studies, we demonstrate that both *Importance Weight* and *Predictor-Corrector-Advancer* contribute significantly to improving model’s performance, underscoring the effectiveness of our design choices in capturing the complex behaviors of turbulent flows. DiffPIR and DPS have large L2 loss and PDE residual, as expected. This can be attributed to using down-sampling to approximate \mathcal{A} and the weaker guidance imposed by these two methods. Although PiRD yields very small PDE residuals for *Taylor-Green Vortex* and *Decaying Turbulence*, these residuals still differ substantially from the high-fidelity reference data. In other words, the method prioritizes reducing the PDE residual at

the expense of predictive accuracy, and the smaller residual does not translate into better flow reconstruction.

Explanation on Large Residual. When you evaluate a PDE residual on a predicted solution, even tiny inaccuracies in your approximation get blown up by the nature of differentiation: taking derivatives accentuates any small noise in the predicted field, turning minute errors into large swings. Further, every PDE comes with an implicit requirement on how many times its solution must be differentiable, so when the predicted flow fields are only piecewise continuous, any discontinuity or abrupt change in slope gets turned into a large error.

Multi-Scale Evaluation. We assess the model’s ability to capture flow structures at different scales using DWT. We present the results on 4× upsampling case in *Kolmogorov Flow* in Table 13 and additional results in Appendix C. SG-Diff demonstrates superior performance in all subdomains. Excelling in the LL subdomain indicates a strong capability in capturing large-scale, low-frequency components of the turbulent flows. The superior performance in the LH and HL subdomains suggests the effectiveness of SG-Diff in capturing small-scale vortices and transitions between scales.

Runtime Comparison. We report the runtime comparison of different methods in Appendix E. SG-Diff only increases small inference time while achieving superior performance improvement against baselines. The total runtime of using the numerical solvers to generate low-fidelity data, and reconstructing with SG-Diff is considerably faster than DNS. Note that numerical solvers employs adaptive time stepping governed by Courant–Friedrichs–Lewy (CFL) condition [5].

Sensitivity Analysis. We study the effects of three key hyperparameters in calculating the importance weight: the maximum importance weight β , minimum importance weight α , and the threshold parameter θ . The results in Appendix F show that increasing β reduces both L2 and PDE residuals, indicating a broader range of importance weights is beneficial. Smaller α values improve performance while setting α to 1 is suboptimal. This can be understood as it decreases the difference between high-frequency and low-frequency regions, as the weight for the latter one is set to 1. Additionally, a larger θ (0.7 or 0.8) helps the model focus on important details. The experiments presented in Appendix F are conducted on the validation datasets for *Kolmogorov Flow*. The optimal hyperparameters, selected based on this validation dataset, are applied across all datasets during testing.

Model	4× Upsampling			8× Upsampling		
	PSNR	SSIM	LPIPS	PSNR	SSIM	LPIPS
DiffPIR	22.6139	0.0512	0.2318	21.5010	0.0394	0.6607
DPS	22.7173	0.0530	0.2148	22.7461	0.0532	0.6606
ResShift	24.4684	0.5587	0.1350	19.1656	0.3099	0.3343
PiRD	23.4082	0.5378	0.1625	19.8004	0.3242	0.3657
RSGD	25.0200	0.6416	0.1233	20.6228	0.3608	0.2915
Diffusion	25.4049	0.6487	0.1215	21.5818	0.4072	0.2848
Cond Diff	25.2389	0.6456	0.1229	20.2067	0.3425	0.2869
SG-Diff	26.1733	0.6781	0.1097	24.0754	0.4409	0.2781

Table 4: PSNR, SSIM and LPIPS scores on *Kolmogorov Flow* for 4× and 8× upsampling.

Image Similarity Metrics. We also evaluate the mode on Learned Perceptual Image Patch Similarity (LPIPS) score [48], Peak Signal-to-Noise Ratio (PSNR) [9], and Structural Similarity Index Measure (SSIM) [42]. We present the results on *Kolmogorov Flow* in Table 4. Additional results on other datasets are presented in Appendix D. Results show that SG-Diff demonstrate superior performance in these metrics under all settings.

Model Generalization. We observe that SG-Diff generalizes well to low-fidelity data generated with different solver configurations. The experiment results are reported in Appendix G. We generate new *Kolmogorov Flow* datasets by varying solver configurations. We compare our model trained with the original *Kolmogorov Flow* datasets with our model trained directly on the new datasets. Results show that our model trained on the original datasets has comparable performance.

4.4 Physical Guidance

We conduct systematic study on how to schedule the corrector. The experiments are conducted on the validation datasets for *Kolmogorov Flow*. The optimal hyperparameters, selected based on this validation dataset, are applied across all datasets during testing.

Schedule	32×32 → 256×256		64×64 → 256×256	
	L2	Res.	L2	Res.
Uniform 4	2.7910	0.1628	1.6645	0.0226
Start 3 End 1	2.7906	0.5913	1.6617	0.1206
Start 2 End 2	2.7897	0.4391	1.6609	0.4309
Start 1 End 3	2.7896	2.183	1.6617	2.1352
Start 4 Space 1	2.7889	10.3074	1.6587	11.4666
Start 4 Space 2	2.7888	9.4531	1.6590	10.4516
Start 4 Space 3	2.7887	9.4531	1.6594	8.6455
End 4 Space 1	2.7930	0.0400	1.6668	0.0080
End 4 Space 2	2.7932	0.0743	1.6747	0.0172
End 4 Space 3	2.7924	0.0407	1.6730	0.0031

Table 5: Scheduling policy comparison on *Kolmogorov Flow*. Applying corrector at the end leads to a reduced PDE residual, while placing it at the beginning achieves a lower L2 loss.

Scheduling Policy. We first explore the optimal schedule policy by comparing: 1.) *Uniform N*: Distributing N residual correction steps evenly across diffusion steps; 2.) *Start I, End N*: Placing I consecutive correction steps at the start and N at the end of the diffusion process; 3.) *Start N, Space S*: Placing N correction steps at the start with a spacing of S ; 4.) *End N, Space S*: Placing N correction steps at the end with a spacing of S . Results in Table 5 suggest that applying correction steps at the beginning achieves the lowest L2, while applying at the end has the lowest PDE residuals. To balance between L2 and PDE residual, we adopt the *Start N End N* schedule.

Number of Correction Steps. We vary the number of N in the *Start N, End N* policy as shown in Figure 3. We observe that increasing N leads to enhanced physical coherence measured by PDE residuals. However, L2 does not continuously decrease with larger N . It reaches a minimum when $N = 2$. This suggests that while more correction steps improve models’ adherence to physical laws, an excessive number may interfere with the model’s ability

to accurately capture the intricate details of the turbulent flow. Therefore, we use *Start 2, End 2* as the optimal balance.

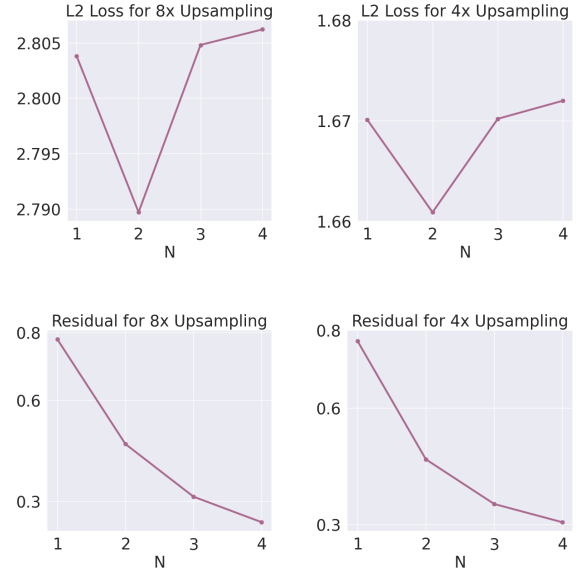


Figure 3: Varying number of N using the *Start N, End N* correction schedule on the *Kolmogorov Flow* dataset. Showing both L2 and Residual across upsampling settings.

5 Conclusion

We study a novel problem of reconstructing high-fidelity CFD from solver-generated low-fidelity inputs. Our diffusion model, SG-Diff, achieves high-quality reconstruction guided by *Importance Weight* and *Predictor-Corrector-Advancer* solver.

6 Limitations

Although the proposed diffusion framework achieves a significant speedup compared to high-fidelity solvers, it remains relatively slow compared to direct mapping models. Future work could explore recent advancements in accelerating diffusion sampling, such as Lu et al. [21], to further enhance the efficiency of the reconstruction process.

7 Broader Impacts

By enhancing the accuracy of CFD simulations, this approach can significantly reduce the computational costs associated with high-resolution simulations, which are often prohibitively expensive in terms of both time and resources. This has implications for a wide range of industries, including aerospace, automotive design, and environmental engineering, where high-fidelity simulations are essential for optimizing performance, safety, and sustainability. Additionally, by improving the quality of low-resolution CFD data, our work could enable more accessible, efficient research and development processes, allowing smaller organizations and research teams to leverage advanced simulation capabilities.

8 Acknowledgments

This work was partially supported by National Artificial Intelligence Research Resource (NAIRR) Pilot (240280, 240443), National Science Foundation (2106859, 2211557, 2119643, 2200274, 2303037, 2312501, 2531008), National Institutes of Health (U54HG012517, U24DK097771, U54OD036472, OT2OD038003, R01HL175135), NEC, Optum AI, SRC JUMP 2.0 Center, Amazon Research Awards, and Snapchat Gifts.

References

- [1] Ali N. Akansu and Richard A. Haddad. 1992. *Multiresolution Signal Decomposition: Transforms, Subbands, and Wavelets*. Academic Press, San Diego, CA.
- [2] Jan-Hendrik Bastek, WaiChing Sun, and Dennis Kochmann. 2025. Physics-Informed Diffusion Models. In *The Thirteenth International Conference on Learning Representations*. <https://openreview.net/forum?id=tpYeermigp>
- [3] Jooyoung Choi, Sungwon Kim, Yonghyun Jeong, Youngjune Gwon, and Sungho Yoon. 2021. ILVR: Conditioning Method for Denoising Diffusion Probabilistic Models. arXiv:2108.02938 [cs.CV] <https://arxiv.org/abs/2108.02938>
- [4] Hyungjin Chung, Jeongsol Kim, Michael Thompson McCann, Marc Louis Klasky, and Jong Chul Ye. 2023. Diffusion Posterior Sampling for General Noisy Inverse Problems. In *The Eleventh International Conference on Learning Representations*. <https://openreview.net/forum?id=OnD9zGAGT0k>
- [5] Richard Courant, Kurt Friedrichs, and Hans Lewy. 1928. Über die partiellen Differenzgleichungen der mathematischen Physik. *Math. Ann.* 100, 1 (1928), 32–74.
- [6] Ingrid Daubechies. 1992. *Ten Lectures on Wavelets*. SIAM, Philadelphia, PA.
- [7] Cong Fu, Jacob Helwig, and Shuiwang Ji. 2023. Semi-Supervised Learning for High-Fidelity Fluid Flow Reconstruction. In *The Second Learning on Graphs Conference*. <https://openreview.net/forum?id=695IYJh1Ba>
- [8] Kai Fukami, Koji Fukagata, and Kunihiko Taira. 2019. Super-resolution reconstruction of turbulent flows with machine learning. *Journal of Fluid Mechanics* 870 (2019), 106–120. doi:10.1017/jfm.2019.238
- [9] Rafael C. Gonzalez and Richard E. Woods. 2002. *Digital Image Processing* (2nd ed.). Prentice Hall.
- [10] Jonathan Ho, Ajay Jain, and Pieter Abbeel. 2020. Denoising Diffusion Probabilistic Models. *arXiv preprint arxiv:2006.11239* (2020).
- [11] Jiaye Huang, Guandao Yang, Zichen Wang, and Jeong Joon Park. 2024. DiffusionPDE: Generative PDE-Solving Under Partial Observation. arXiv:2406.17763 [cs.LG] <https://arxiv.org/abs/2406.17763>
- [12] Zijie Huang, Yizhou Sun, and Wei Wang. 2023. Generalizing graph ode for learning complex system dynamics across environments. In *Proceedings of the 29th ACM SIGKDD Conference on Knowledge Discovery and Data Mining*. 798–809.
- [13] Chiyu Max Jiang, Soheil Esmailzadeh, Kamyar Azizzadenesheli, Karthik Kashinath, Mustafa A. Mustafa, Hamdi A. Techelepi, Philip S. Marcus, Prabhath, and Anima Anandkumar. 2020. MESHFREEFLOWNET: A Physics-Constrained Deep Continuous Space-Time Super-Resolution Framework. *SC20: International Conference for High Performance Computing, Networking, Storage and Analysis* (2020), 1–15. <https://api.semanticscholar.org/CorpusID:218487006>
- [14] Bahjat Kawar, Michael Elad, Stefano Ermon, and Jiaming Song. 2022. Denoising Diffusion Restoration Models. In *Advances in Neural Information Processing Systems*.
- [15] Diederik P. Kingma and Jimmy Ba. 2015. Adam: A Method for Stochastic Optimization. *International Conference on Learning Representations (ICLR)* (2015). <https://arxiv.org/abs/1412.6980>
- [16] Matthew Li and Christopher McComb. 2022. Using Physics-Informed Generative Adversarial Networks to Perform Super-Resolution for Multiphase Fluid Simulations. *Journal of Computing and Information Science in Engineering* 22, 4 (02 2022), 044501. arXiv:https://asmedigitalcollection.asme.org/computingengineering/article-pdf/22/4/044501/6850327/jcise_22_4_044501.pdf doi:10.1115/1.4053671
- [17] Ruoyan Li, Dipti Ranjan Sahu, Guy Van den Broeck, and Zhe Zeng. 2025. Deep Generative Models with Hard Linear Equality Constraints. arXiv:2502.05416 [cs.LG] <https://arxiv.org/abs/2502.05416>
- [18] Ruoyan Li, Guancheng Wan, Zijie Huang, Zixiao Liu, Haixin Wang, Xiao Luo, Wei Wang, and Yizhou Sun. 2025. Flow Field Reconstruction with Sensor Placement Policy Learning. In *The Thirty-ninth Annual Conference on Neural Information Processing Systems*. <https://openreview.net/forum?id=1esFEjMUBS>
- [19] Zongyi Li, Nikola Kovachki, Kamyar Azizzadenesheli, Burigede Liu, Kaushik Bhat-tacharya, Andrew M Stuart, and Anima Anandkumar. 2020. Fourier neural operator for parametric partial differential equations. *arXiv preprint arXiv:2010.08895* (2020).
- [20] Zongyi Li, Hongkai Zheng, Nikola Kovachki, David Jin, Haoxuan Chen, Burigede Liu, Kamyar Azizzadenesheli, and Anima Anandkumar. 2023. Physics-Informed Neural Operator for Learning Partial Differential Equations. arXiv:2111.03794 [cs.LG] <https://arxiv.org/abs/2111.03794>
- [21] Cheng Lu, Yuhao Zhou, Fan Bao, Jianfei Chen, Chongxuan Li, and Jun Zhu. 2022. DPM-Solver: A Fast ODE Solver for Diffusion Probabilistic Model Sampling in Around 10 Steps. *arXiv preprint arXiv:2206.00927* (2022).
- [22] Lu Lu, Pengzhan Jin, and George Em Karniadakis. 2019. DeepONet: Learning nonlinear operators for identifying differential equations based on the universal approximation theorem of operators. *arXiv preprint arXiv:1910.03193* (2019).
- [23] Andreas Lugmayr, Martin Danelljan, Andres Romero, Fisher Yu, Radu Timofte, and Luc Van Gool. 2022. RePaint: Inpainting using Denoising Diffusion Probabilistic Models. arXiv:2201.09865 [cs.CV] <https://arxiv.org/abs/2201.09865>
- [24] Gisiro Maruyama. 1955. Continuous Markov processes and stochastic equations. *Rendiconti del Circolo Matematico di Palermo* 4 (1955), 48–90.
- [25] James C. McWilliams. 1984. The emergence of isolated coherent vortices in turbulent flow. *Journal of Fluid Mechanics* 146 (1984), 21–43. doi:10.1017/S0022112084001750
- [26] Chenlin Meng, Yutong He, Yang Song, Jiaming Song, Jiajun Wu, Jun-Yan Zhu, and Stefano Ermon. 2022. SDEdit: Guided Image Synthesis and Editing with Stochastic Differential Equations. In *International Conference on Learning Representations*.
- [27] Steven A. Orszag. 1972. Comparison of Pseudospectral and Spectral Approximation. *Studies in Applied Mathematics* 51, 3 (September 1972), 253–259. doi:10.1002/sapm1972513253
- [28] Anirudhe Pradhan and Karthik Duraisamy. 2021. Variational Multi-scale Super-resolution: A data-driven approach for reconstruction and predictive modeling of unresolved physics. arXiv:2101.09839 [physics.comp-ph] <https://arxiv.org/abs/2101.09839>
- [29] Jing Qiu, Jiancheng Huang, Xiangdong Zhang, Zeng Lin, Minglei Pan, Zengding Liu, and Fen Miao. 2024. Pi-fusion: Physics-informed diffusion model for learning fluid dynamics. arXiv:2406.03711 [physics.flu-dyn] <https://arxiv.org/abs/2406.03711>
- [30] Pu Ren, Chengping Rao, Yang Liu, Zihan Ma, Qi Wang, Jian-Xun Wang, and Hao Sun. 2023. PhysSR: Physics-informed deep super-resolution for spatiotemporal data. *J. Comput. Phys.* 492 (2023), 112438. doi:10.1016/j.jcp.2023.112438
- [31] François Rozet and Gilles Louppe. 2023. Score-based Data Assimilation. In *Thirty-seventh Conference on Neural Information Processing Systems*. <https://openreview.net/forum?id=VUVLSnMZdX>
- [32] Chitwan Saharia, Jonathan Ho, William Chan, Tim Salimans, David J Fleet, and Mohammad Norouzi. 2021. Image super-resolution via iterative refinement. *arXiv:2104.07636* (2021).
- [33] Chitwan Saharia, Jonathan Ho, William Chan, Tim Salimans, David J Fleet, and Mohammad Norouzi. 2022. Image super-resolution via iterative refinement. *IEEE TPAMI* (2022).
- [34] Rajat Kumar Sarkar, Ritam Majumdar, Vishal Jadhav, Sagar Srinivas Sakhinana, and Venkataramana Runkana. 2023. Redefining Super-Resolution: Fine-mesh PDE predictions without classical simulations. arXiv:2311.09740 [physics.flu-dyn] <https://arxiv.org/abs/2311.09740>
- [35] Siming Shan, Pengkai Wang, Song Chen, Jiayu Liu, Chao Xu, and Shengze Cai. 2024. PiRD: Physics-informed Residual Diffusion for Flow Field Reconstruction. arXiv:2404.08412 [physics.flu-dyn] <https://arxiv.org/abs/2404.08412>
- [36] Dule Shu, Zijie Li, and Amir Barati Farimani. 2023. A Physics-informed Diffusion Model for High-fidelity Flow Field Reconstruction. *J. Comput. Phys.* (2023), 111972.
- [37] Yang Song, Jascha Sohl-Dickstein, Diederik P Kingma, Abhishek Kumar, Stefano Ermon, and Ben Poole. 2021. Score-Based Generative Modeling through Stochastic Differential Equations. In *International Conference on Learning Representations*. <https://openreview.net/forum?id=PxTIG12RRHS>
- [38] Haixin Wang, Yadi Cao, Zijie Huang, Yuxuan Liu, Peiyan Hu, Xiao Luo, Zeheng Song, Wanxia Zhao, Jilin Liu, Jinan Sun, et al. 2024. Recent Advances on Machine Learning for Computational Fluid Dynamics: A Survey. *arXiv preprint arXiv:2408.12171* (2024).
- [39] Haixin Wang, Ruoyan Li, Fred Xu, Fang Sun, Kaiqiao Han, Zijie Huang, Guancheng Wan, Ching Chang, Xiao Luo, Wei Wang, and Yizhou Sun. 2025. FD-Bench: A Modular and Fair Benchmark for Data-driven Fluid Simulation. arXiv:2505.20349 [physics.flu-dyn] <https://arxiv.org/abs/2505.20349>
- [40] Qi Wang, Yuan Mi, Wang Haoyun, Yi Zhang, Ruizhi Chengze, Hongsheng Liu, Ji-Rong Wen, and Hao Sun. 2025. MultiPDENet: PDE-embedded Learning with Multi-time-stepping for Accelerated Flow Simulation. In *Forty-second International Conference on Machine Learning*. <https://openreview.net/forum?id=D1gs8QT74m>
- [41] Yinhuai Wang, Jiwen Yu, and Jian Zhang. 2023. Zero-Shot Image Restoration Using Denoising Diffusion Null-Space Model. *The Eleventh International Conference on Learning Representations* (2023).
- [42] Zhou Wang, Alan C. Bovik, Hamid R. Sheikh, and Eero P. Simoncelli. 2004. Image Quality Assessment: From Error Visibility to Structural Similarity. *IEEE Transactions on Image Processing* 13, 4 (2004), 600–612. doi:10.1109/TIP.2003.819861
- [43] Jonas Bernhard Wildberger, Maximilian Dax, Simon Buchholz, Stephen R Green, Jakob H. Macke, and Bernhard Schölkopf. 2023. Flow Matching for Scalable Simulation-Based Inference. In *Thirty-seventh Conference on Neural Information*

- Processing Systems*. <https://openreview.net/forum?id=D2cS6SoYIP>
- [44] Gefan Yang and Stefan Sommer. 2023. A Denoising Diffusion Model for Fluid Field Prediction. arXiv:2301.11661 [cs.LG] <https://arxiv.org/abs/2301.11661>
 - [45] Ling Yang and Shenda Hong. 2022. Unsupervised Time-Series Representation Learning with Iterative Bilinear Temporal-Spectral Fusion.
 - [46] Sihyun Yu, Jihoon Tack, Sangwoo Mo, Hyunsu Kim, Junho Kim, Jung-Woo Ha, and Jinwoo Shin. 2022. Generating Videos with Dynamics-aware Implicit Generative Adversarial Networks. In *International Conference on Learning Representations*.
 - [47] Zongsheng Yue, Jianyi Wang, and Chen Change Loy. 2023. ResShift: Efficient Diffusion Model for Image Super-resolution by Residual Shifting. arXiv:2307.12348 [cs.CV] <https://arxiv.org/abs/2307.12348>
 - [48] Richard Zhang, Phillip Isola, Alexei A. Efros, Eli Shechtman, and Oliver Wang. 2018. The Unreasonable Effectiveness of Deep Features as a Perceptual Metric. In *Proceedings of the IEEE Conference on Computer Vision and Pattern Recognition (CVPR)*, 586–595.
 - [49] Yi Zhang, Dapeng Zhang, and Haoyu Jiang. 2023. Review of challenges and opportunities in turbulence modeling: A comparative analysis of data-driven machine learning approaches. *Journal of Marine Science and Engineering* 11, 7 (2023), 1440.
 - [50] Anthony Zhou, Zijie Li, Michael Schneier, John R Buchanan Jr, and Amir Barati Farimani. 2025. Text2PDE: Latent Diffusion Models for Accessible Physics Simulation. In *The Thirteenth International Conference on Learning Representations*. <https://openreview.net/forum?id=Nb3a8aUGfj>
 - [51] Yuanzhi Zhu, Kai Zhang, Jingyun Liang, Jiezhong Cao, Bihan Wen, Radu Timofte, and Luc Van Gool. 2023. Denoising Diffusion Models for Plug-and-Play Image Restoration. In *IEEE Conference on Computer Vision and Pattern Recognition Workshops (NTIRE)*.

A Dataset

All datasets are generated using pseudo-spectral solver. The time-stepping method employed is a combination of the Crank-Nicholson scheme and Heun’s method. For numerical stability, the solver uses an adaptive time-stepping approach governed by the Courant-Friedrichs-Lewy (CFL) condition. The CFL condition ensures that the time step remains sufficiently small relative to the velocity field and the external forcing, preventing instabilities that can arise from rapid changes in the solution. Additionally, the dealiasing procedure, using the 2/3 rule, removes high-frequency components from the Fourier spectrum, ensuring that non-physical aliasing effects are avoided.

Algorithm 2 Pseudo-spectral Navier-Stokes Solver

```

1: Input: Initial vorticity  $\omega_0$ , forcing  $f$ , Reynolds number  $Re$ , total
   time  $T$ , timestep  $\Delta t$ , domain size  $L_1, L_2$ , grid size  $s_1, s_2$ , adaptivity
   flag
2: Output: Vorticity  $\omega$  at time  $T$ 
3: Initialize: Compute wavenumbers, Laplacian, and dealiasing
   mask
4:
5: while  $t < T$  do
6:   if adaptive then
7:     Compute velocity field  $\mathbf{u} = \nabla^\perp \psi$ 
8:     Update timestep  $\Delta t$  based on CFL
9:   end if
10:  Compute non-linear term in Fourier space
11:  Predictor and corrector steps using Crank-Nicholson + Heun

12:  Apply dealiasing mask
13:  Update time  $t = t + \Delta t$ 
14: end while
15: Return Vorticity  $\omega$ 

```

Taylor Green Vortex The initial vorticity field is based on the analytical solution of the TGV, and to generate different trajectories, we added random perturbations from a Gaussian random field. These perturbations introduce variability to the initial conditions while maintaining the overall vortex structure. No external forcing was applied during the simulation, and the spatial domain is $[0, \frac{3}{2}\pi]^2$ with a fixed Reynolds number of 1000. The simulation used a time step $dt = \frac{1}{32}$, and 100 trajectories were generated each with a total duration of $T = 6$ seconds. The initial vorticity field is based on the analytical solution for the two-dimensional periodic domain. The vorticity field ω is initialized as $\omega = -2U_0k \sin(kx) \sin(ky)$, where U_0 is the initial velocity amplitude, and k is the wave number that determines the size of the vortices. To introduce variability and generate different trajectories, a Gaussian Random Field is added as a perturbation to the initial vorticity.

Decaying Turbulence The spatial domain is $[0, 1]^2$, with periodic boundary conditions and a fixed Reynolds number of 450. The simulation used a time step $dt = \frac{1}{32}$, and 400 trajectories were generated, each with a total duration of $T = 2$ seconds. The initial conditions for the decaying turbulence dataset are generated by superimposing randomly positioned vortices of varying intensity and size. Each vortex is characterized by a randomly selected core

size and maximum rotational velocity, allowing for a diverse range of initial flow structures. The vortices are distributed randomly throughout the domain, and their periodic images are added to ensure the proper enforcement of periodic boundary conditions.

Kolmogorov Flow The initial vorticity field is generated using a Gaussian random field, and the system is subjected to a forcing term of the form $f(\mathbf{x}) = -4 \cos(4x_2) - 0.1\omega(\mathbf{x}, t)$. This forcing drives the flow in the y-direction while introducing a drag force that dissipates energy. The spatial domain is $[0, 2\pi]^2$, with a fixed Reynolds number of 1000. The simulation used a time step $dt = \frac{1}{32}$, and 50 trajectories were generated, each with a total duration of $T = 10$ seconds. The initial vorticity field is produced by sampling from a Gaussian Random Field. As the external forcing continually adds energy to the system, the initially simple vorticity evolves into intricate and turbulent structures. The vorticity is allowed to evolve over a 5-second period, and the final state at the end of this interval is used as the initial condition for our dataset.

McWilliams Flow The phenomenon illustrates the emergence of order from initially disordered turbulent motion, driven by viscous dissipation and the self-organization of the flow. No external forcing is applied during the simulation, allowing for a natural decay and evolution of the turbulence. The spatial domain is $[0, 2\pi]^2$, with periodic boundary conditions and a Reynolds number of 2000, providing a high degree of turbulence. The simulation used a time step $dt = \frac{1}{32}$, and 50 trajectories were generated, each with a total duration of $T = 10$ seconds. The initial vorticity field for the *McWilliams Flow* is generated following the method described by McWilliams [25]. The process begins by constructing a Fourier mesh over the spatial domain, where the wavenumbers k_x and k_y are calculated. A scalar wavenumber function is prescribed, and the ensemble variance is determined to ensure that the energy distribution in Fourier space follows the desired spectral shape. Random Gaussian perturbations are applied to each Fourier component of the stream function, producing a random realization of the vorticity field. To ensure the stream function has a zero mean, a spectral filter is applied, and the field is normalized based on the kinetic energy. Finally, the vorticity field is computed in physical space by taking the inverse Laplacian of the stream function in Fourier space, resulting in a turbulent flow field that evolves naturally without external forcing.

B Experiment Results for Direct Mapping Models

For direct mapping models, we compare against a CNN-based model [8], a GAN-based model [16]. Note that we apply 5 steps of gradient descent using the residual to the reconstructed sample to enhance physical consistency. The results are reported in Table 6.

	Metric	CNN	GAN
Taylor Green Vortex	L2	3.66	3.53
	Res.	139.7468	1.7611
	L2	2.69	0.9990
	Res.	52661.27	0.7642
Decaying Turbulence	L2	2.01	2.09
	Res.	82.1334	6.7948
	L2	1.40	2.04
	Res.	57.1200	4.1499
McWilliams Flow & Kolmogorov Flow	L2	3.41	3.11
	Res.	515.8137	69.5502
	L2	3.13	3.04
	Res.	185.4361	62.6224
	L2	2.31	2.20
	Res.	654.7895	1533.1234
	L2	1.61	1.92
	Res.	712.5844	1540.6807

Table 6: Quantitative performance comparison over four datasets on L2 and Res. Metrics are reported for both $32 \times 32 \rightarrow 256 \times 256$ (gray) and $64 \times 64 \rightarrow 256 \times 256$ tasks.

C Multi-Scale Evaluation

Table 7: Kolmogorov Flow $8 \times$ Upsampling

Method	HH	HL	LL	LH
DiffPIR	4.3914	9.0811	188.6012	3.6674
DPS	4.3914	9.0795	188.0532	3.6646
ResShift	0.0722	1.8942	39.4973	2.1263
PiRD	0.0649	1.8410	37.2648	2.0639
RSGD	0.0346	0.2947	40.0763	0.4904
Diffusion	0.0382	0.2935	41.8237	0.4429
Cond Diff	0.0344	0.2903	42.9040	0.4445
SG-Diff	0.0312	0.2616	33.8086	0.3798

Table 8: McWilliams Flow $4 \times$ Upsampling

Method	HH	HL	LL	LH
DiffPIR	0.4226	1.1473	75.6783	0.5940
DPS	0.4225	1.1465	75.4513	0.5932
ResShift	0.0523	0.9234	6.8736	0.8362
PiRD	0.0516	0.9271	6.8646	0.8350
RSGD	0.0203	0.2155	6.6627	0.1959
Diffusion	0.0182	0.2108	6.7780	0.1834
Cond Diff	0.0167	0.2229	6.8123	0.1944
SG-Diff	0.0141	0.1642	6.2937	0.1452

Table 9: McWilliams Flow $8 \times$ Upsampling

Method	HH	HL	LL	LH
DiffPIR	0.4182	1.1362	75.4749	0.6381
DPS	0.4225	1.1468	75.4864	0.5934
ResShift	0.0320	0.9873	19.3344	0.9170
PiRD	0.0321	0.9917	19.4258	0.9253
RSGD	0.0152	0.2288	23.2287	0.1983
Diffusion	0.0152	0.2287	20.9631	0.2027
Cond Diff	0.0151	0.2353	21.1752	0.2085
SG-Diff	0.0145	0.1920	17.4284	0.1708

Table 10: Decaying Turbulence $4 \times$ Upsampling

Method	HH	HL	LL	LH
DiffPIR	5.9452	9.0297	35.3487	3.7063
DPS	5.9452	9.0292	35.3019	3.7059
ResShift	0.0504	0.7032	5.1194	0.7208
PiRD	0.0500	0.7140	5.3197	0.7326
RSGD	0.0442	0.0611	7.4907	0.0431
Diffusion	0.0765	0.0995	5.1389	0.0994
Cond Diff	0.0365	0.0510	29.6782	0.0546
SG-Diff	0.0196	0.0264	5.0720	0.0267

Table 11: Decaying Turbulence $8 \times$ Upsampling

Method	HH	HL	LL	LH
DiffPIR	5.9592	9.0601	52.0273	3.7367
DPS	5.9592	9.0600	52.0212	3.7366
ResShift	0.0416	1.1680	26.8325	1.2171
PiRD	0.0416	1.1843	26.7621	1.2353
RSGD	0.0425	0.0508	29.0300	0.0896
Diffusion	0.1780	0.2204	25.0249	0.2159
Cond Diff	0.0461	0.0511	34.5407	0.0591
SG-Diff	0.0238	0.0488	24.1640	0.0512

Table 12: Taylor Green Vortex $4 \times$ Upsampling

Method	HH	HL	LL	LH
DiffPIR	19.4488	42.9432	127.4038	5.5207
DPS	19.4477	42.9413	127.1114	5.5192
ResShift	0.3451	1.3825	13.0696	1.3727
PiRD	0.3422	1.3822	20.4812	1.3618
RSGD	0.3385	0.5539	27.0561	0.4622
Diffusion	0.1703	0.2959	11.3933	0.2928
Cond Diff	0.2941	0.5003	77.4125	0.4899
SG-Diff	0.1507	0.2928	9.3202	0.2903

Table 13: Taylor Green Vortex 8× Upsampling

Method	HH	HL	LL	LH
DiffPIR	19.4647	42.9816	141.3724	5.5507
DPS	19.4671	42.9863	141.0834	5.5499
ResShift	0.2900	1.9425	44.7676	1.9238
PiRD	0.2811	1.9054	66.0041	1.8890
RSGD	0.0284	0.4015	84.0803	0.3705
Diffusion	0.0998	0.3941	44.8146	0.3727
Cond Diff	0.0174	0.3832	81.7034	0.3772
SG-Diff	0.0172	0.3811	41.5014	0.3704

D Image Similarity Metrics

Although LPIPS is trained on the ImageNet dataset, which consists of natural images, it remains a valuable metric for evaluating perceptual quality in CFD applications. This is because LPIPS leverages features from deep neural networks that are effective at capturing multi-scale patterns, textures, and perceptual similarities, regardless of the specific domain. Fluid dynamics data often have complex structures and turbulent patterns that share characteristics with textures found in natural images, making LPIPS suitable for assessing the fidelity of reconstructed flow fields. Thus, despite being trained on ImageNet, LPIPS can still effectively quantify how well the reconstructed samples retain important perceptual details, making it a robust metric for evaluating the visual quality of CFD reconstructions.

Model	8× Upsampling	4× Upsampling
DiffPIR	0.5993	0.2139
DPS	0.5993	0.2148
ResShift	0.3748	0.1747
PiRD	0.3684	0.1689
RSGD	0.3511	0.1498
Diff	0.3524	0.1457
Cond Diff	0.3540	0.1604
SG-Diff	0.2936	0.1298

Table 14: LPIPS scores on McWilliams Flow.

Model	8× Upsampling	4× Upsampling
DiffPIR	0.6616	0.6525
DPS	0.2148	0.2148
ResShift	0.2231	0.2514
PiRD	0.2262	0.2524
RSGD	0.1639	0.2115
Diff	0.4215	0.3608
Cond Diff	0.1688	0.2259
SG-Diff	0.1397	0.0637

Table 15: LPIPS scores on Decaying Turbulence.

Model	8× Upsampling	4× Upsampling
DiffPIR	0.5785	0.5702
DPS	0.2148	0.2148
ResShift	0.2559	0.3899
PiRD	0.2881	0.2478
RSGD	0.2148	0.1813
Diff	0.2525	0.1494
Cond Diff	0.1750	0.2362
SG-Diff	0.1704	0.1339

Table 16: LPIPS scores on Taylor Green Vortex.

The PSNR and SSIM results are reported below:

McWilliams Flow				
Model	4x Upsampling		8x Upsampling	
	PSNR	SSIM	PSNR	SSIM
DiffPIR	20.7069	0.0426	20.2405	0.0381
DPS	18.5968	0.0257	18.7903	0.0270
ResShift	28.7484	0.5945	20.3056	0.2827
PiRD	25.2076	0.5110	20.2050	0.2784
RSGD	26.5900	0.6088	21.6394	0.3056
Diffusion	29.7101	0.6686	25.2200	0.3884
Cond Diff	29.6757	0.6665	25.1475	0.3823
SG-Diff	30.0540	0.6722	28.1972	0.4643

Taylor Green Vortex				
Model	4x Upsampling		8x Upsampling	
	PSNR	SSIM	PSNR	SSIM
DiffPIR	30.0668	0.7328	20.2300	0.6633
DPS	30.3133	0.7261	23.2857	0.7373
ResShift	30.5201	0.8009	23.7859	0.6162
PiRD	28.3752	0.7028	22.1947	0.4981
RSGD	25.0744	0.7933	20.9531	0.5955
Diffusion	30.7706	0.8438	24.8698	0.6678
Cond Diff	23.2154	0.6767	21.3979	0.5959
SG-Diff	31.5277	0.8713	26.7503	0.7562

Decaying Turbulence				
Model	4x Upsampling		8x Upsampling	
	PSNR	SSIM	PSNR	SSIM
DiffPIR	31.7640	0.5763	30.3585	0.5160
DPS	31.0463	0.5534	30.1307	0.5088
ResShift	29.0554	0.7998	23.6247	0.5798
PiRD	21.2584	0.7215	27.7594	0.6512
RSGD	40.5449	0.9259	35.3302	0.8185
Diffusion	47.2289	0.9571	40.8901	0.8622
Cond Diff	46.0675	0.9138	40.1089	0.8456
SG-Diff	48.0321	0.9601	43.0276	0.9295

E Runtime Comparison

Table 17 presents the time required for the numerical solver to generate a single frame of low- and high-fidelity samples for each dataset. Note that adaptive time stepping with CFL condition is adopted to ensure numerical stability. The high-fidelity data 256×256 are generated using 4096×4096 and then downsampled to 256×256 . All datasets are generated using pseudo spectral solver that run on GPU.

Dataset	256×256	64×64	32×32
<i>Kolmogorov Flow</i>	246.23	0.44	0.04
<i>McWilliams Flow</i>	156.20	1.23	0.12
<i>Decaying Turbulence</i>	151.70	1.01	0.06
<i>Taylor Green Vortex</i>	247.03	1.49	0.22

Table 17: Run time of numerical solver to generate one frame for each dataset across different grid resolutions with a batch size of 10. All times are measured in seconds.

Table 18 shows the time comparison across ML models for reconstructing high-fidelity data from low-fidelity inputs.

Method	$32 \times 32 \rightarrow 256 \times 256$	$64 \times 64 \rightarrow 256 \times 256$
DiffPIR	17.27	17.27
DPS	17.11	17.11
ResShift	3.96	3.96
PiRD	5.15	5.15
RSGD	6.13	3.14
Diff	6.10	3.06
Cond Diff	6.20	3.38
SG-Diff	6.37	3.27

Table 18: Runtime comparison of various methods across different resolution levels using a batch size of 10, with all times measured in seconds.

F Importance Weight Sensitivity Analysis

We present a sensitivity analysis to explore how different hyperparameter settings affect the performance of the Importance Weight Strategy. The importance weight strategy is governed by three main parameters: β (the maximum importance weight), α (the minimum importance weight), and θ (the importance threshold). We adjust these parameters sequentially. The results are summarized in Figure 4.

G Generalization

We observe that SG-Diff generalizes well to low-fidelity data generated with different solver configurations. We conduct evaluations over three generalization settings: time discretization, spatial domain size, and Reynolds number as shown in Table 19. We train SG-Diff on the original *Kolmogorov Flow* dataset, which has timestep $dt = 1/32$, spatial domain size $2\pi \times 2\pi$, and Reynolds number $Re = 1000$. We then directly test these new low-fidelity data on the trained model, without any additional retraining or fine-tuning. We

compare the performance against models directly trained on each new configuration.

The results reveal that the pertained SG-Diff performs comparably to trained ones directly on each new configuration. This underscores our model’s strong generalization capabilities across different solver configurations. Such generalization ability is particularly important given the high-level objective is to combine SG-Diff with solvers operating on coarser grids to generate high-fidelity data faster. The generalization ability can be due to the fact that both our *importance weight* mechanism and *residual correction* modules are training-free. They enable our model to locate fine-grained high-fidelity details and adhere to physical laws independent of training data. A similar trend is also observed in $4\times$ upsampling experiments.

Variation	Model	L2	Res.
Time Discretization Variations			
$dt = 1/40$	Trained on Original Data	2.8144	0.0497
	Trained on $dt = 1/40$ Data	2.8136	0.0474
$dt = 1/50$	Trained on Original Data	2.7761	0.0253
	Trained on $dt = 1/50$ Data	2.7795	0.0939
Spatial Domain Size Variations			
$1\pi \times 1\pi$	Trained on Original Data	1.9045	2.4468
	Trained on $1\pi \times 1\pi$ Data	1.7672	1.1074
$1.5\pi \times 1.5\pi$	Trained on Original Data	2.3573	0.6852
	Trained on $1.5\pi \times 1.5\pi$ Data	2.3028	1.0282
Reynolds Number Variations			
$Re = 500$	Trained on Original Data	2.3694	0.2058
	Trained on $Re = 500$ Data	2.3542	0.1513
$Re = 2000$	Trained on Original Data	3.2957	0.2113
	Trained on $Re = 2000$ Data	3.2914	0.2406

Table 19: Generalization results on *Kolmogorov Flow* dataset with $32 \times 32 \rightarrow 256 \times 256$ setting.

Table 20: Generalization results on *Kolmogorov Flow* dataset with $64 \times 64 \rightarrow 256 \times 256$ setting.

Variation	Model	L2	Res.
Time Discretization Variations			
$dt = 1/40$	Trained on Original Data	1.6782	0.0820
	Trained on $dt = 1/40$ Data	1.6723	0.0897
$dt = 1/50$	Trained on Original Data	1.6484	0.0581
	Trained on $dt = 1/50$ Data	1.6489	0.1567
Spatial Domain Size Variations			
$1\pi \times 1\pi$	Trained on Original Data	1.0255	2.4649
	Trained on $1\pi \times 1\pi$ Data	0.9443	1.3626
$1.5\pi \times 1.5\pi$	Trained on Original Data	1.3212	0.8261
	Trained on $1.5\pi \times 1.5\pi$ Data	1.2918	1.3220
Reynolds Number Variations			
$Re = 500$	Trained on Original Data	1.3112	0.2613
	Trained on $Re = 500$ Data	1.2998	0.2301
$Re = 2000$	Trained on Original Data	1.9647	0.2066
	Trained on $Re = 2000$ Data	1.9694	0.2035

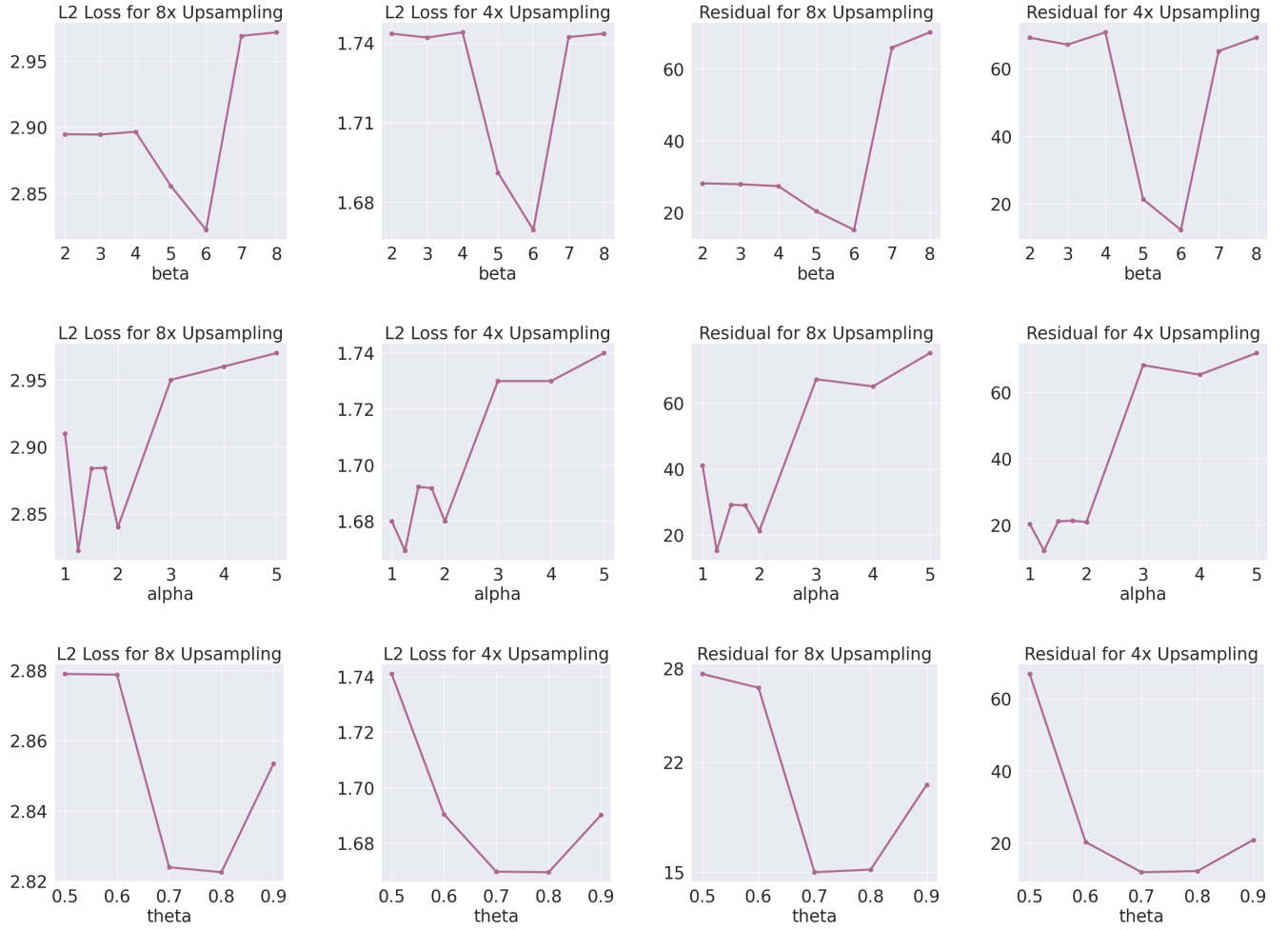


Figure 4: Sensitivity analysis of key parameters for the *Importance Weight*. Experiments are conducted on the *Kolmogorov Flow*. The top row presents the results for the maximum importance weight, β . The middle row displays the results for the minimum importance weight, α , and the bottom row shows the results for the importance threshold, θ . These three hyperparameters were tuned in sequence, and the optimal combination ($\beta = 6$, $\alpha = 1.25$, and $\theta = 0.8$) is selected.

H Proof of Proposition 3.3

Give the Predictor-Corrector-Advancer SDE solver as follows:

- Predictor $\tilde{x}_0^t = \text{NN}_\theta(x_t, t)$
- Corrector $\tilde{x}_0^t = C(\tilde{x}_0^t)$ if correction is applied else $\bar{x}_0^t = \tilde{x}_0^t$
- Advancer $x_{t-1} = x_t + \left[f(x_t, t) + g^2(t) \frac{x_t - \tilde{x}_0^t - \int_0^t f(x_s, s) ds}{\int_0^t g^2(s) ds} \right] dt + g(t) d\bar{W}$

We can consider the SDE of interest to be

$$dx = \left[f(x, t) + g^2(t) \frac{x_t - \tilde{x}_0^t - \int_0^t f(x, s) ds}{\int_0^t g^2(s) ds} \right] dt + g(t) d\bar{W}$$

Define $\bar{f}(x, t) = f(x, t) + g^2(t) \frac{x_t - \tilde{x}_0^t - \int_0^t f(x, s) ds}{\int_0^t g^2(s) ds}$ and $\bar{g}(t) = g(t)$.

Assumption H.1. Let $f(x, t)$ and $g(t)$ be the drift function and diffusion coefficient of VP-SDE [10]. Then, $f(x, t)$ is Lipschitz with respect to x with Lipschitz constant L_f .

Then, if \hat{x}_t denotes the piecewise constant solution, for $0 \leq t \leq T$,

$$\begin{aligned} Z(t) &= \sup_{0 \leq s \leq t} \mathbb{E} [|x_s - \hat{x}_s|^2] \\ &= \sup_{0 \leq s \leq t} \mathbb{E} \left| \int_0^{t_{ns}} \bar{f}(x_u, t_u) - \bar{f}(\hat{x}_u, t_u) du \right. \\ &\quad \left. + \int_0^{t_{ns}} \bar{g}(t_u) - \bar{g}(t_u) dW_u \right. \\ &\quad \left. + \int_{t_{ns}}^s \bar{f}(\hat{x}_u, t_u) du + \int_{t_{ns}}^s \bar{g}(t_u) dW_u \right|^2 \\ &= \sup_{0 \leq s \leq t} \mathbb{E} \left| \int_0^{t_{ns}} \bar{f}(x_u, t_u) - \bar{f}(\hat{x}_u, t_u) du \right. \\ &\quad \left. + \int_{t_{ns}}^s \bar{f}(\hat{x}_u, t_u) du + \int_{t_{ns}}^s \bar{g}(t_u) dW_u \right|^2 \end{aligned}$$

By Cauchy Schwarz inequality

$$\begin{aligned} &\leq 3 \sup_{0 \leq s \leq t} \mathbb{E} \left| \int_0^{t_{ns}} \bar{f}(x_u, t_u) - \bar{f}(\hat{x}_u, t_u) du \right|^2 \\ &\quad + \left| \int_{t_{ns}}^s \bar{f}(\hat{x}_u, t_u) du \right|^2 + \left| \int_{t_{ns}}^s \bar{g}(t_u) dW_u \right|^2 \end{aligned}$$

By linearity of expectation, Ito's isometry, and Cauchy Schwarz inequality,

$$\begin{aligned} &\leq 3 \sup_{0 \leq s \leq t} T \mathbb{E} \left[\int_0^{t_{ns}} |\bar{f}(x_u, t_u) - \bar{f}(\hat{x}_u, t_u)|^2 du \right] \\ &\quad + \Delta t \mathbb{E} \left[\int_{t_{ns}}^s |\bar{f}(\hat{x}_u, t_u)|^2 du \right] + \mathbb{E} \left[\int_{t_{ns}}^s |\bar{g}(t_u)|^2 du \right] \end{aligned}$$

Note that in $\bar{f}(x_t, t) = f(x_t, t) + g^2(t) \frac{x_t - \bar{x}_0 - \int_0^t f(x_s, s) ds}{\int_0^t g^2(s)}$, $f(x_t, t)$ is Lipschitz with respect to x_t by construction. $g^2(t)$, $\int_0^t f(x_s, s) ds$, and $\int_0^t g^2(s)$ are constant with respect to x_t .

Assumption H.2. The predictor $\bar{x}_0^t = NN_\theta(x_t, t)$ is Lipschitz with Lipschitz constant L_{NN} .

The Lipschitz assumption for the predictor is simply requiring the gradient with respect to the input x_t to be bounded. This is a necessary condition for training NN_θ .

Assumption H.3. Let \mathcal{R} be the PDE residual. Then, $\nabla \mathcal{R}(x)$ and $\nabla^2 \mathcal{R}(x)$ are bounded within the domain of interest. Further, $\nabla \mathcal{R}(x)$ is Lipschitz with respect to x with Lipschitz constant $L_{\mathcal{R}}$.

The corrector $\bar{x}_0^t = C(\bar{x}_0^t)$ involves M steps of gradient descent using the gradient of the PDE residual. In the context of PDEs—particularly for the turbulent Navier–Stokes equations—this assumption may not hold due to the inherently irregular and multi-scale nature of turbulent flows. Despite this, Shu et al. [36] incorporate $\nabla \mathcal{R}(x)$ as an input to the denoiser, a procedure that necessitates the boundedness of both $\nabla \mathcal{R}(x)$ and $\nabla^2 \mathcal{R}(x)$ to ensure stable gradient propagation. Consequently, we adopt the assumption that $\nabla \mathcal{R}(x)$ and $\nabla^2 \mathcal{R}(x)$ are bounded within the domain of interest.

For the Adam gradient descent, $m_{t+1} = \beta_1 m_t + (1 - \beta_1) \nabla \mathcal{R}(x_t)$ and $v_{t+1} = \beta_2 v_t + (1 - \beta_2) (\nabla \mathcal{R}(x_t))^2$. The update rule can be written

as $x_{t+1} = x_t - \eta Q(m_{t+1}, v_{t+1})$ with $Q(m, v) = \frac{m}{\sqrt{v + \epsilon}}$.

$$\frac{\partial Q}{\partial \nabla \mathcal{R}} = \frac{\frac{\partial m}{\partial \nabla \mathcal{R}} (\sqrt{v} + \epsilon) + m \frac{1}{2} v^{-1/2} \frac{\partial v}{\partial \nabla \mathcal{R}}}{(\sqrt{v} + \epsilon)^2}$$

Using the boundedness of $\nabla \mathcal{R}$ and the Adam parameters, Q is Lipschitz with respect to $\partial \nabla \mathcal{R}$ and assume the Lipschitz constant is L_Q . Then, Q is Lipschitz with respect to x with Lipschitz constant $L_Q L_{\mathcal{R}}$. As a result, the one step gradient descent $T(x) = x - \eta Q(x)$ has Lipschitz constant $1 + \eta L_Q L_{\mathcal{R}}$. By induction, M steps of gradient descent has Lipschitz constant $(1 + \eta L_Q L_{\mathcal{R}})^M$.

As a result, The corrector can also be considered as Lipschitz with Lipschitz constant $L_{\bar{f}} = L_f + \frac{|\sup_{0 \leq s \leq T} g^2(s)|}{|\sup_{0 \leq s \leq T} \int_0^s g^2(s)|} (1 + (1 + \eta L_Q L_{\mathcal{R}})^M L_{NN})$ if correction is applied and $\hat{L}_{\bar{f}} = L_f + \frac{|\sup_{0 \leq s \leq T} g^2(s)|}{|\sup_{0 \leq s \leq T} \int_0^s g^2(s)|} (1 + L_{NN})$ otherwise. Note that since $(1 + \eta L_Q L_{\mathcal{R}})^M > 1$, $L_{\bar{f}} > \hat{L}_{\bar{f}}$.

Let $A \cup B = [0, t_{ns}]$ and $A \cap B = \emptyset$. Let A denotes the set where correction is applied and B denotes the set where correction is not applied. Then,

$$\begin{aligned} &\int_0^{t_{ns}} |\bar{f}(x_u, t_u) - \bar{f}(\hat{x}_u, t_u)|^2 du \\ &= \int_A |\bar{f}(x_u, t_u) - \bar{f}(\hat{x}_u, t_u)|^2 du + \int_B |\bar{f}(x_u, t_u) - \bar{f}(\hat{x}_u, t_u)|^2 du \\ &\leq L_{\bar{f}} \int_A |x_u - \hat{x}_u|^2 du + \hat{L}_{\bar{f}} \int_B |x_u - \hat{x}_u|^2 du \end{aligned}$$

Define $\alpha = \frac{\int_A |x_u - \hat{x}_u|^2 du}{\int_0^{t_{ns}} |x_u - \hat{x}_u|^2 du} \propto |A|$. Then, $1 - \alpha = \frac{\int_B |x_u - \hat{x}_u|^2 du}{\int_0^{t_{ns}} |x_u - \hat{x}_u|^2 du} \propto |B|$. We have,

$$\leq (\alpha L_{\bar{f}} + (1 - \alpha) \hat{L}_{\bar{f}}) \int_0^{t_{ns}} |x_u - \hat{x}_u|^2 du$$

Then we have

$$\begin{aligned} &\leq 3 \sup_{0 \leq s \leq t} (\alpha L_{\bar{f}} + (1 - \alpha) \hat{L}_{\bar{f}})^2 T \mathbb{E} \left[\int_0^{t_{ns}} |x_u - \hat{x}_u|^2 du \right] \\ &\quad + \Delta t \mathbb{E} \left[\int_{t_{ns}}^s |\bar{f}(\hat{x}_u, t_u)|^2 du \right] + \mathbb{E} \left[\int_{t_{ns}}^s |\bar{g}(t_u)|^2 dW_u \right] \\ &\leq 3 \sup_{0 \leq s \leq t} ((\alpha L_{\bar{f}} + (1 - \alpha) \hat{L}_{\bar{f}})^2 T \int_0^{t_{ns}} Z(u) du \\ &\quad + \Delta t \mathbb{E} \left[\int_{t_{ns}}^s |\bar{f}(\hat{x}_u, t_u)|^2 du \right] + C) \end{aligned}$$

where $C \Delta t = \mathbb{E} \left[\int_{t_{ns}}^s |\bar{g}(t_u)|^2 dW_u \right]$. The Lipschitz condition of $\bar{f}(x, t)$ implies the linear growth condition. There exists K_f such that $|\bar{f}(x, t)| \leq K_f (1 + |x|)$.

$$\begin{aligned}
&\leq 3 \sup_{0 \leq s \leq t} (\alpha L_{\bar{f}} + (1 - \alpha) \hat{L}_{\bar{f}})^2 T \int_0^{t_{ns}} Z(u) du \\
&+ K_f^2 \Delta t \mathbb{E} \left[\int_{t_{ns}}^s |1 + |x_u||^2 du \right] + C \Delta t \\
&\leq 3 \sup_{0 \leq s \leq t} (\alpha L_{\bar{f}} + (1 - \alpha) \hat{L}_{\bar{f}})^2 T \int_0^{t_{ns}} Z(u) du \\
&+ \Delta t \left[K_f \left(\Delta t + \int_{t_{ns}}^s \mathbb{E} [|x_u|^2] \right) + C \right] \\
&\leq 3((\alpha L_{\bar{f}} + (1 - \alpha) \hat{L}_{\bar{f}})^2 T \int_0^{t_{ns}} Z(u) du \\
&+ \Delta t \left[K_f^2 \Delta t \left(1 + \sup_{0 \leq t \leq T} \mathbb{E} [|x_t|^2] \right) + C \right])
\end{aligned}$$

As a condition for the existence of strong solution, we assume $\sup_{0 \leq t \leq T} \mathbb{E} [|x_t|^2] \leq D$. Then,

$$\begin{aligned}
&\leq 3((\alpha L_{\bar{f}} + (1 - \alpha) \hat{L}_{\bar{f}})^2 T \int_0^{t_{ns}} Z(u) du \\
&+ \Delta t \left[K_f^2 \Delta t \left(1 + \sup_{0 \leq t \leq T} \mathbb{E} [|x_t|^2] \right) + C \right])
\end{aligned}$$

By Grönwall's inequality,

$$\begin{aligned}
Z(T) &= \sup_{0 \leq s \leq T} \mathbb{E} [|x_s - \hat{x}_s|^2] \\
&\leq \Delta t \left[K_f^2 \Delta t (1 + D) + C \right] \exp(3(\alpha L_{\bar{f}} + (1 - \alpha) \hat{L}_{\bar{f}})^2 T^2)
\end{aligned}$$

Now, notice that

$$\begin{aligned}
\alpha &= \frac{\int_A |x_u - \hat{x}_u|^2 du}{\int_0^{t_{ns}} |x_u - \hat{x}_u|^2 du} \\
&\leq \frac{|A| \sup_{0 \leq u \leq t_{ns}} |x_u - \hat{x}_u|^2}{t_{ns} \inf_{0 \leq u \leq t_{ns}} |x_u - \hat{x}_u|^2} = c_1 |A|
\end{aligned}$$

Additionally,

$$\begin{aligned}
\alpha &= \frac{\int_A |x_u - \hat{x}_u|^2 du}{\int_0^{t_{ns}} |x_u - \hat{x}_u|^2 du} \\
&\geq \frac{|A| \inf_{0 \leq u \leq t_{ns}} |x_u - \hat{x}_u|^2}{t_{ns} \sup_{0 \leq u \leq t_{ns}} |x_u - \hat{x}_u|^2} = c_2 |A|
\end{aligned}$$

Thus, $\alpha = O(|A|)$ and $\alpha^2 = O(|A|^2)$. Next, we notice that

$$\begin{aligned}
L_{\bar{f}} &= \hat{L}_{\bar{f}} + \Delta L \\
\Delta L &= \frac{|\sup_{0 \leq s \leq T} g^2(s)|}{|\sup_{0 \leq s \leq T} \int_0^s g^2(s)|} (1 + (1 + \eta L_Q L_{\mathcal{R}})^M L_{\text{NN}}) + (L_f - \hat{L}_{\bar{f}})
\end{aligned}$$

Thus,

$$\Delta L = O((1 + \eta L_Q L_{\mathcal{R}})^M)$$

Plug in ΔL into $\Lambda = \alpha L_{\bar{f}} + (1 - \alpha) \hat{L}_{\bar{f}}$. We get

$$\begin{aligned}
\Lambda &= \hat{L}_{\bar{f}} + \alpha \Delta L \\
\Lambda^2 &= \hat{L}_{\bar{f}}^2 + 2\alpha \hat{L}_{\bar{f}} \Delta L + \alpha^2 \Delta L^2 \\
\Lambda^2 &\leq c_3 \alpha^2 \Delta L^2 = O(|A|^2 (1 + \eta L_Q L_{\mathcal{R}})^{2M})
\end{aligned}$$

Thus,

$$\begin{aligned}
Z(T) &= \sup_{0 \leq s \leq T} \mathbb{E} [|x_s - \hat{x}_s|^2] \\
&= O(\Delta t \exp(O(|A|^2 (1 + \eta L_Q L_{\mathcal{R}})^{2M})))
\end{aligned}$$

I Hardware Specification

We implement all models in PyTorch. All experiments are run on servers/workstations with the following configuration:

- 80 CPUs, 503G Mem, 8 x NVIDIA V100 GPUs.
- 48 CPUs, 220G Mem, 8 x NVIDIA TITAN Xp GPUs.
- 96 CPUs, 1.0T Mem, 8 x NVIDIA A100 GPUs.
- 64 CPUs, 1.0T Mem, 8 x NVIDIA RTX A6000 GPUs.
- 224 CPUs, 1.5T Mem, 8 x NVIDIA L40S GPUs.